Tricuspid valve maladaptation in sheep with biventricular heart failure: The posterior and septal leaflets

Colton J Kostelnik[1,†], **William D Meador**[1,†], **Chien-Yu Lin**[1], **Mrudang Mathur**[2], **Marcin Malinowski**[3,4], **Tomasz Jazwiec**[3,5], **Zuzanna Malinowska**[6], **Magda L Piekarska**[3,4], **Boguslaw Gaweda**[3], **Tomasz A Timek**[3], **Manuel K. Rausch***[1,2,6]

***For correspondence:** manuel.rausch@utexas.edu (MKR)

[†]These authors contributed equally to this work

Present address: 2617 Wichita Street, Austin, TX 78712

[1]Department of Biomedical Engineering, The University of Texas at Austin, Austin, United States; [2]Department of Mechanical Engineering, The University of Texas at Austin, Austin, United States; [3]Division of Cardiothoracic Surgery, Corewell Health, Grand Rapids, United States; [4]Department of Cardiac Surgery, Medical University of Silesia, School of Medicine in Katowice, Katowice, Poland; [5]Department of Cardiac, Vascular, and Endovascular Surgery and Transplantology, Medical University of Silesia in Katowice, Silesian Centre for Heart Disease, Zabrze, Poland; [6]Department of Aerospace Engineering and Engineering Mechanics, The University of Texas at Austin, Austin, United States

Abstract Tricuspid valve leaflets are dynamic tissues that can remodel in response to altered biomechanical and hemodynamic loads. The anterior, posterior, and septal leaflets exhibit distinct morphology, composition, and mechanical properties, resulting in varying in vivo strains. We hypothesized that these differences would result in leaflet-specific remodeling changes in a sheep model of biventricular heart failure. Previously, we reported significant maladaptive changes in the anterior leaflet (***Meador et al., 2020b***). Here, we extended the analysis to the posterior and septal leaflets and observed a lesser but notable remodeling response. Both the diseased posterior and septal leaflets showed increased free edge thickness and valvular interstitial cell activation. However, only the posterior leaflet exhibited increased circumferential stiffness and collagen content. In contrast, only the septal leaflet increased in area and displayed signs of endothelial-to-mesenchymal transition. These findings emphasize the importance of considering leaflet-specific remodeling when developing computational models or targeted treatment strategies for tricuspid valve disease.

Introduction

Tricuspid regurgitation (TR) is a highly prevalent echocardiographic finding that is detectable in 82-86% of people (***Singh et al., 1999***). Approximately 1.6 million Americans suffer from moderate to severe TR, which if left untreated, can lead to multiple cardiovascular complications (***Enriquez-Sarano et al., 2019***). More than 90% of patients with severe TR exhibit a "functional" etiology, wherein the valve dysfunction is secondary to other cardiac pathologies such as left-sided heart disease or pulmonary hypertension (***Condello et al., 2021***; ***Fender et al., 2018***; ***Henning, 2022***). The

valve itself is believed to be structurally and mechanically intact, and this assumption has guided a conservative treatment approach that focuses on managing the primary condition to resolve any TR (***Lee et al., 2019***; ***Taramasso et al., 2012***). However, early surgical repair of the tricuspid valve during mitral or aortic valve surgeries has shown promise in improving patient outcomes and diminishing cardiac-related mortality (***Rogers and Bolling, 2009***; ***Pagnesi et al., 2017***). Despite this evolution of TR management, it remains under-treated and poorly understood.

Heart valve leaflets were once considered "passive flaps" that merely coordinated unidirectional blood flow between the heart chambers. However, we now know that heart valve leaflets are highly organized tissues with multiple cell types and intricate extracellular architectures that actively remodel by contracting and reshaping to optimize coaptation (***Grande-Allen et al., 2005b***; ***Chaput et al., 2008***; ***Itoh et al., 2009***). In diseased patients, leaflet remodeling induces a fibrotic response (i.e., maladapt), which impedes proper kinematics and coaptation (***Grande-Allen et al., 2005a***). Animal studies of heart failure and chronic ischemia have shown that maladaptive changes in the mitral valve leaflets manifest by increased size, thickness, and stiffness (***Rausch et al., 2012***; ***Timek et al., 2006***). We have demonstrated in two animal models that similar remodeling patterns exist in the tricuspid valve leaflets (e.g., increases in area, thickness, and stiffness) in response to altered biomechanical and hemodynamic loads (***Meador et al., 2020b***; ***Iwasieczko et al., 2023a***). These remodeling-induced leaflet changes affect leaflet stresses and valve contact area, indicating that valve function is sensitive to this leaflet maladaptation (***Mathur et al., 2024***).

We have shown that the tricuspid leaflets from healthy sheep exhibit drastically different morphology, mechanical properties, and in vivo area strains (***Meador et al., 2020a***; ***Mathur et al., 2019***). These leaflet-specific properties suggest that each leaflet has the potential to manifest maladaptive remodeling changes differently. In our previous study, we determined that the anterior tricuspid leaflet exhibited maladaptive changes on all functional scales (***Meador et al., 2020b***). Here, we aimed to quantify the maladaptive changes in the posterior and septal tricuspid leaflets from the same sheep with biventricular heart failure after 2-3 weeks of tachycardia-induced cardiomyopathy (TIC). Based on the in vivo strains from healthy sheep, we hypothesize that these maladaptive remodeling changes seen in the anterior leaflets of TIC animals will also be present but to a lesser extent in the posterior and septal leaflets. We hypothesize that the TIC posterior and septal leaflets will undergo remodeling localized to regions of high strains (i.e., posterior belly and septal free edge). This distinction of differential remodeling may be vital in informing models of disease progression and could provide future therapeutic targets.

Results and Discussion

TIC-induced changes to posterior and septal leaflet geometry and mechanics

Leaflet geometry is an important determinant for assessing valve function in TR (***Afilalo et al., 2015***). Our previous study found significant changes in the anterior leaflet geometry in TIC animals (***Meador et al., 2020b***). Building on our previous studies in tricuspid valve leaflets, we hypothesized that TIC animals would show an increase in leaflet area for both the posterior and septal leaflets, and only the septal leaflet would increase in thickness. Towards testing these hypotheses, we quantified the posterior and septal leaflet morphology and thicknesses in TIC animals (***Figure 1***a, ***Figure 2***a, ***Figure 2***d, respectively). Posterior leaflet morphology remained unchanged between TIC and control (CTL) animals (***Figure 1***(b-d)). In contrast, the TIC septal leaflets significantly increased in leaflet area (134%, $p = 0.001$, ***Figure 1***e) and leaflet height (111%, $p = 0.040$, ***Figure 1***f). Posterior leaflet free edge thickness significantly increased by (160%) ($p = 0.010$, ***Figure 2***b), and septal leaflet free edge thickness significantly increased by (130%) ($p = 0.050$, ***Figure 2***e). However, when summarized into a single average thickness, we failed to find any significant increase in either the TIC posterior and septal leaflets (***Figure 2***c & ***Figure 2***f).

Leaflet remodeling in heart failure patients has influenced leaflet mechanics (***Grande-Allen et al., 2005a***). Our previous study demonstrated that the anterior tricuspid leaflet mechanical

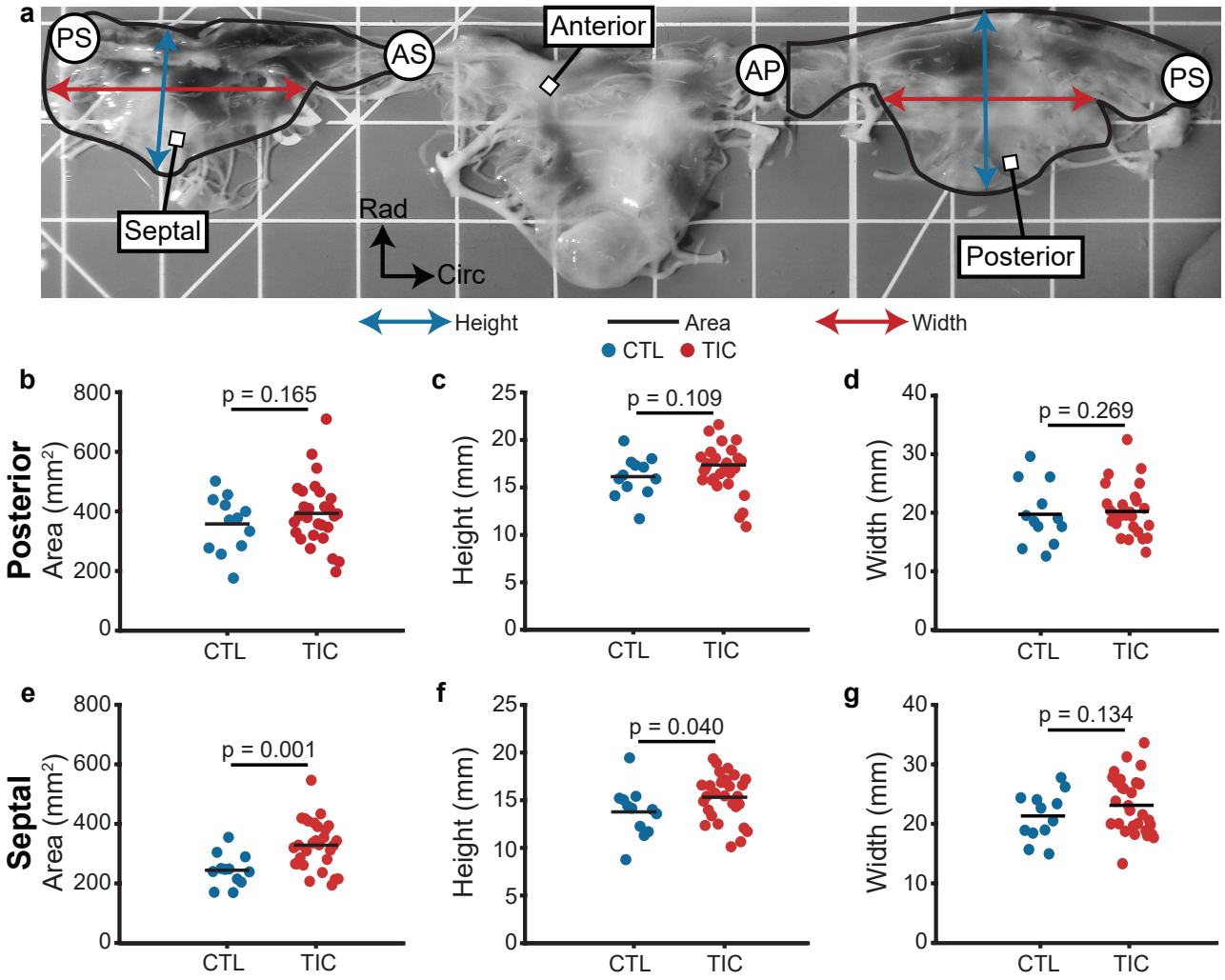

Figure 1. Tricuspid valve septal leaflet area increases in sheep with tachycardia-induced cardiomyopathy (TIC). (a) An image of a sheep tricuspid valve separated at the posterior-septal (PS) commissure was captured on a calibrated grid. The measured area (black), height (blue), and width (red) are shown on the posterior and septal leaflets. The posterior leaflet area was measured from the antero-posterior (AP) commissure to the PS commissure, while the septal leaflet area was measured from the PS commissure to the antero-septal (AS) commissures. Grid-scale = 1 cm. (b-d) Comparisons between posterior control (CTL, blue, n = 12) and TIC (red, n = 29) (b) area, (c) height, and (d) width. (e-g) Comparisons between the septal control (CTL, blue, n = 12) and TIC (red, n = 29) (e) area, (f) height, and (g) width. Black bars represent the data mean if normal or the data median if non-normal, as determined by Shapiro-Wilk's normality test. The p-values compare the morphological measurements between CTL and TIC for respective posterior and septal leaflets using the Student's t-test when normally distributed or the Wilcoxon Rank-Sum test when non-normally distributed.

properties were significantly altered in diseased animals (***Meador et al., 2020b***). Similar to the anterior leaflet, we hypothesized that the TIC posterior and septal leaflets would exhibit a stiffer and more isotropic behavior. Here, both posterior and septal leaflets exhibited the classic J-shaped loading curve of biological collagenous tissues (***Figure 3***a & ***Figure 3***d). Our biaxial mechanical analysis found that TIC posterior leaflet stiffness significantly increased at large stretches (i.e., calf stiffness) in the circumferential direction (p = 0.022) but failed to detect a significant change in the septal leaflets (***Figure 3***b & ***Figure 3***e, respectively). We failed to detect any significant change in the stiffness at small stretches (i.e., toe stiffness) for both the posterior and septal leaflets (***Figure 3***c & ***Figure 3***f, respectively). Posterior leaflet anisotropy and transition stretches were consistent between CTL and TIC animals (***Figure 4***a-b), whereas the septal leaflets showed a significant increase in radial transition stretch (p = 0.031) and a significant decrease in anisotropy (p = 0.005) in TIC

animals (***Figure 4***c-d).

Distinct morphological and mechanical properties in tricuspid leaflets are essential for maintaining healthy valve function (***Meador et al., 2020a***; ***Laurence et al., 2019***). Our geometric and mechanical analysis highlights the heterogeneous remodeling response in diseased tricuspid valve leaflets on the tissue level. The substantial increase in septal leaflet area, particularly height, suggests a compensatory mechanism to accommodate the increased septal-lateral annular dilation (***Iwasieczko et al., 2023b***). Similarly, the free edge thickening of both leaflets likely reflects adaptive responses to tethering forces(***Dal-Bianco et al., 2009***). For instance, in vivo strain data from healthy sheep highlight regions subjected to high strain during normal cardiac cycles. (***Mathur et al., 2019***). The posterior leaflet belly experiences greater area strains than the septal leaflet, whereas the septal leaflet free edge experiences greater area strains than the posterior. This distinction in belly region strains may explain the increased stiffness observed in the posterior leaflet but not the septal leaflet. This stiffness increase could be attributed to RV enlargement tethering the posterior chordae and contributing to higher circumferential stresses (***Rogers and Bolling, 2009***). Interestingly, while the CTL septal leaflet exhibited near-isotropic behavior, the TIC septal leaflet showed a trend toward greater anisotropy, aligning more with circumferential loading similar to the other two leaflets. This shift likely results from increased septal commissure-commissure distance and septal annular perimeter in TIC animals, imposing greater circumferential stresses on the septal leaflet (***Iwasieczko et al., 2023b***). Additionally, the TIC septal leaflet experienced more stretch along its radial axis (i.e., its axis of growth), suggesting a diminished matrix composition or radially oriented collagen fibers. Overall, these structural and mechanical differences in the posterior and septal leaflets highlight leaflet-specific remodeling, likely influenced by altered RV geometry, annular geometry, and chordal tethering.

Differential expression of cellular remodeling markers in TIC posterior and septal leaflets

Pathogenic activation of valvular endothelial cells (VECs) and valvular interstitial cells (VICs) promotes extracellular matrix remodeling through expression, secretion, and degradation of key load-bearing proteins (***Kodigepalli et al., 2020***). Our previous study observed increased regional expression of remodeling markers (αSMA, Ki67, MMP13 and TGF-β1) in TIC anterior leaflets (***Meador et al., 2020b***). Based on our previous findings that tricuspid leaflets exhibit geometric changes (i.e., area and thickness) in response to disease, we hypothesized that the TIC posterior and septal leaflets would have increased expression of these remodeling markers (***Meador et al., 2020b***; ***Iwasieczko et al., 2023a***). Here, we determined the regional expression of the same remodeling markers in TIC posterior and septal leaflets. In the TIC posterior leaflets, expression of αSMA and Ki67 increased in the near-annulus region (***Figure 5***a-b), which is consistent with the observed increase in cell nuclei density of this region (***Figure 5—figure Supplement 1***). In contrast, the expression levels of MMP13 varied throughout the TIC posterior leaflets, while the expression of TGF-β1 decreased across the TIC posterior leaflets. In the TIC septal leaflets, we observed increased regional expression for all four remodeling markers in the near-annulus and belly region (***Figure 6***). We observed decreased expression of MMP13 in the septal free edge region (***Figure 6***c). In addition, we observed an increase in cell nuclei density within the near-annulus region of the TIC septal leaflets (***Figure 6—figure Supplement 1***).

Different regions of the valve leaflet exhibit distinct behaviors and activation patterns, contributing to regional heterogeneity in remodeling (***Blevins et al., 2008***). The increase of αSMA expression in the near-annulus and free edge regions suggests localized VIC activation. Activated VICs assume a hypersecretory phenotype – known as myofibroblasts – that contributes to fibrosis by secretion of collagen (***Ma et al., 2017***). The decrease of MMP13 expression in the free edge region of the posterior and septal leaflet suggests diminished matrix turnover. The complementary signaling of these remodeling markers agrees with the observed free edge thickening, suggesting upregulated collagen deposition in both TIC posterior and septal leaflets. The localization of both Ki67 and

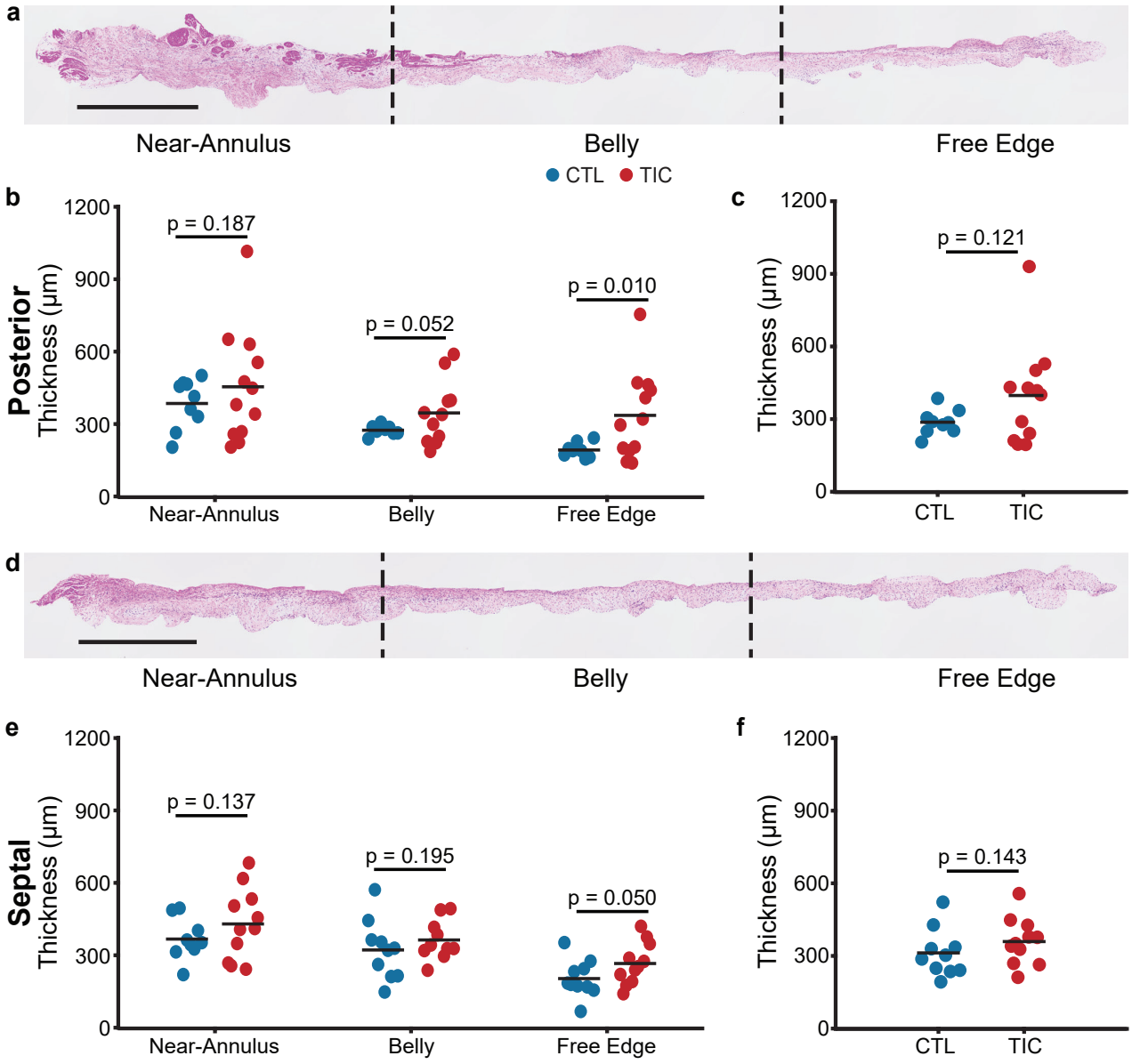

Figure 2. Posterior leaflet free edge thickness increases in tachycardia-induced cardiomyopathy (TIC). Representative images of (a) posterior and (d) septal leaflet strips divided into three equidistant regions (near-annulus, belly, and free edge). Comparisons between control (CTL, blue, n = 9) and TIC (red, n = 12) posterior leaflet thickness when data is (c) regionally assessed and (d) pooled. Comparisons between control (CTL, blue, n = 10) and TIC (red, n = 11) septal leaflet thickness when data is (e) regionally assessed and (f) pooled. Black bars represent the data mean if normal and the data median if non-normal as determined by Shapiro-Wilk's normality test. The p-values compare thicknesses between CTL and TIC within each region for respective posterior and septal leaflets using the Student's t-test when normally distributed or the Wilcoxon Rank-Sum test when non-normally distributed.

TGF-β1 to the endothelial layer of TIC septal leaflets may indicate endothelial-to-mesenchymal transition and highlight the unique roles of endothelial cells in responding to mechanical stress and regulating inflammatory and fibrotic responses (***Figure 6***d) (***Li et al., 2018***). The regional heterogeneous expression of remodeling markers between the posterior and septal leaflets supports that leaflet- and region-specific stimuli, possibly related to mechanical loading or biochemical environment, drive a localized remodeling response (***Grande-Allen and Liao, 2011***).

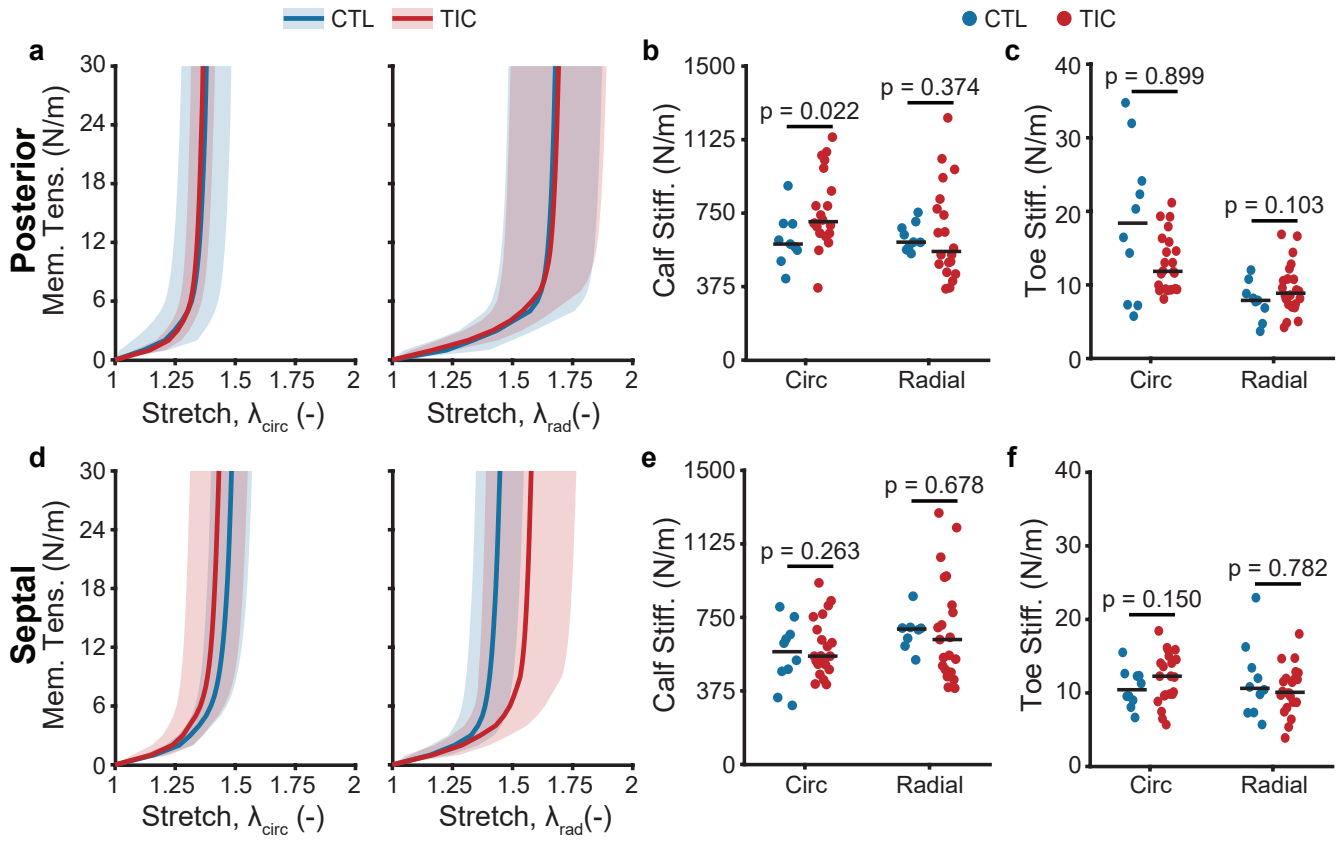

Figure 3. Tachycardia-induced cardiomyopathy (TIC) posterior leaflets are stiffer in the circumferential (circ) directions. Control (CTL, blue, n = 10 for each leaflet) and TIC (red, n = 22 for each leaflet) membrane tension (Mem. Tens.) vs stretch average curves (solid) with standard deviation (shaded) in the circumferential and radial directions for (a) posterior and (d) septal leaflets. Comparisons of the (b & e) stiffness at large stretches (calf stiffness) in the circumferential and radial directions for the posterior and septal leaflets, respectively. Comparisons of the (c & f) stiffness at small stretches (toe stiffness) in the circumferential and radial directions for the posterior and septal leaflets, respectively. Black bars represent the data mean if normal and the data median in non-normal as determined by Shapiro-Wilk's normality test. The p-values compare stiffnesses between CTL and TIC for respective posterior and septal leaflets in both the circumferential and radial directions using the Student's t-test when normally distributed or the Wilcoxon Rank-Sum test when non-normally distributed.

Variation in collagen content and fiber orientation in TIC posterior and septal leaflets

Collagen is a key load-bearing component of the leaflet extracellular matrix (ECM), constituting approximately 90% of its structure (***Kodigepalli et al., 2020***). Previous studies on mitral leaflets and our research on TIC anterior tricuspid leaflets have found that collagen content increases in leaflets from valves with severe regurgitation (***Meador et al., 2020b***; ***Stephens et al., 2009***). Collagen synthesis is associated with large tissue strains, and our earlier work observed in vivo strains localized to the posterior belly and septal free edge in sheep hearts (***Mathur et al., 2019***). Based on this, we hypothesized that the TIC posterior and septal leaflets would have higher collagen content than CTL leaflets, particularly in regions with the greatest in vivo strains. Specifically, we expected increased collagen content in the TIC posterior leaflet belly region and the TIC septal free edge. We observed a significant increase in collagen content in the belly region of the TIC posterior leaflet (142%, p = 0.021, ***Figure 7***a). In the TIC septal leaflets, there were non-significant increases in collagen content in the near-annulus (p = 0.091) and free edge (p = 0.088) regions (***Figure 7***c). When pooling all regions, no significant changes in overall collagen content were found for either the posterior (p = 0.127) or septal (p = 0.484) leaflets (***Figure 7***b and ***Figure 7***d).

Collagen fiber orientation is crucial for maintaining leaflet stiffness during the cardiac cycle (***Hudson et al., 2020***). Our previous study showed increased radially dispersed fibers in the atrialis

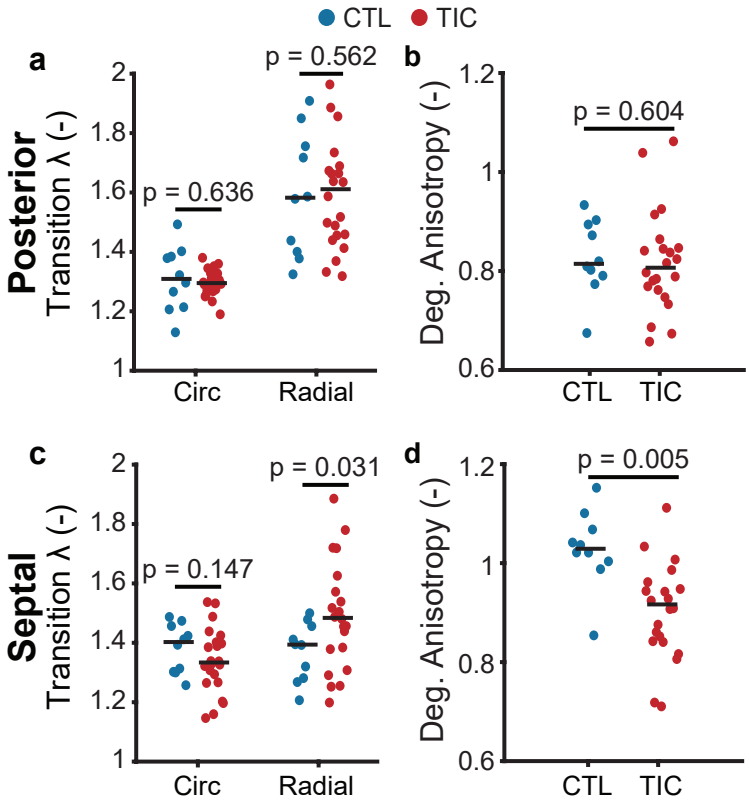

Figure 4. Tachycardia-induced cardiomyopathy (TIC) septal leaflets biaxial curves exhibited increased radial transition stretch and decreased anisotropy. Comparisons of the transition stretch in circumferential and radial directions between control (CTL, blue, n = 10) and TIC (red, n = 22) (a) posterior and (c) septal leaflets. Comparisons of the degree of anisotropy between CTL (blue, n = 10) and TIC (red, n = 22) (b) posterior and (d) septal leaflets. Black bars represent the data mean if normal and the data median in non-normal as determined by Shapiro-Wilk's normality test. The p-values compare circumferential and radial transition stretches and the degree of anisotropy between CTL and TIC for respective posterior and septal leaflets using the Student's t-test when normally distributed or the Wilcoxon Rank-Sum test when non-normally distributed.

region of TIC anterior leaflets (***Meador et al., 2020b***). We hypothesized that the TIC posterior and septal leaflets would show a similar increase in collagen fiber dispersion. To test this, we fit von Mises probability distribution functions to collagen fiber orientation histograms from both leaflets of CTL and TIC animals and (***Figure 8***a, ***Figure 8***c). From this, we quantified the concentration parameter κ and measured fiber dispersion as a function of imaging depth. A large κ value reflects more aligned fibers, while lower values suggest greater dispersion and more isotropic distribution of collagen fibers are more aligned. Our analysis showed that CTL posterior and septal leaflet fibers were circumferentially oriented. We found that this fiber orientation remained consistent in the TIC posterior leaflets ***Figure 8***b. However, we observed a significant decrease in the κ value in the 0-33% (p = 0.020), 34-66% (p = 0.024), and 67-100% (p = 0.009) depth regions of the TIC septal leaflets ***Figure 8***d. Our analysis of cell nuclei orientation, nuclear aspect ratio (NAR), and circularity showed no notable differences between CTL and TIC cell nuclei for the posterior (***Figure 8—figure Supplement 1***) or septal (***Figure 8—figure Supplement 2***) leaflet.

Regional ECM changes in collagen content and fiber dispersion are driven by localized profibrotic cellular responses and degradative enzymes triggered by spatially heterogeneous pathological strains imposed by annular dilation or leaflet tethering (***Grande-Allen and Liao, 2011***; ***Dal-Bianco et al., 2009***). These strains are often localized along the free edge, which may have activated mechanobiological pathways promoting maladaptive remodeling within that region (***Korossis, 2018***; ***Kodigepalli et al., 2020***). Our mechanical results align with our microstructural find-

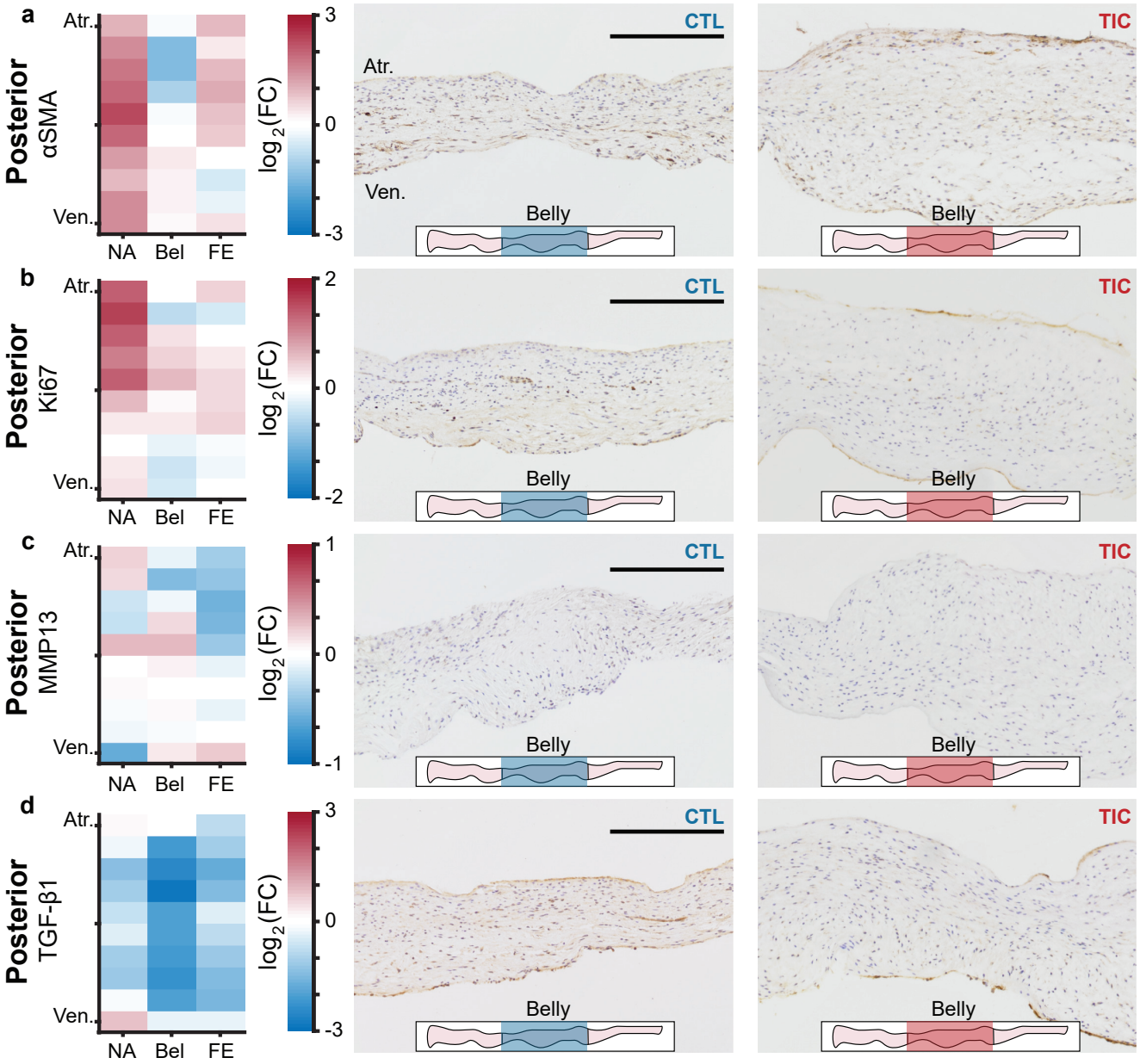

Figure 5. Marginal changes in remodeling cellular markers in tachycardia-induced cardiomyopathy (TIC) posterior leaflets. (a-d) Heat maps (left) showing regional expression of (a) alpha-smooth muscle actin (αSMA), (b) Ki67, (c) matrix metalloproteinase 13 (MMP13), (d) transforming growth factor beta (TGF-β1). The heatmaps are separated into three equidistant regions along the radial axis (near-annulus (NA), belly (Bel), free edge (FE)) and 10 thickness regions from the atrialis side (Atr.) to the ventricularis side (Ven.). Fold change (FC) between control (CTL, n = 6) and TIC (n = 6) was determined by the ratio of positively stained pixel percentage between TIC and CTL. Color map indicates the logarithm base 2 of the fold change, interpreted as (positive, red): TIC expression is higher than CTL, (0, white): TIC and CTL expression are approximately equal, and (negative, blue): TIC expression is less than CTL. Representative images of CTL (middle) and TIC(right) posterior leaflets are shown with the atrialis surface upward. The inset leaflet schematic depicts the longitudinal region from which the representative image was taken. Scale bars = 500 μm.

Figure 5—figure supplement 1. Cellular nuclei density increases along ventricularis side of posterior TIC leaflets.

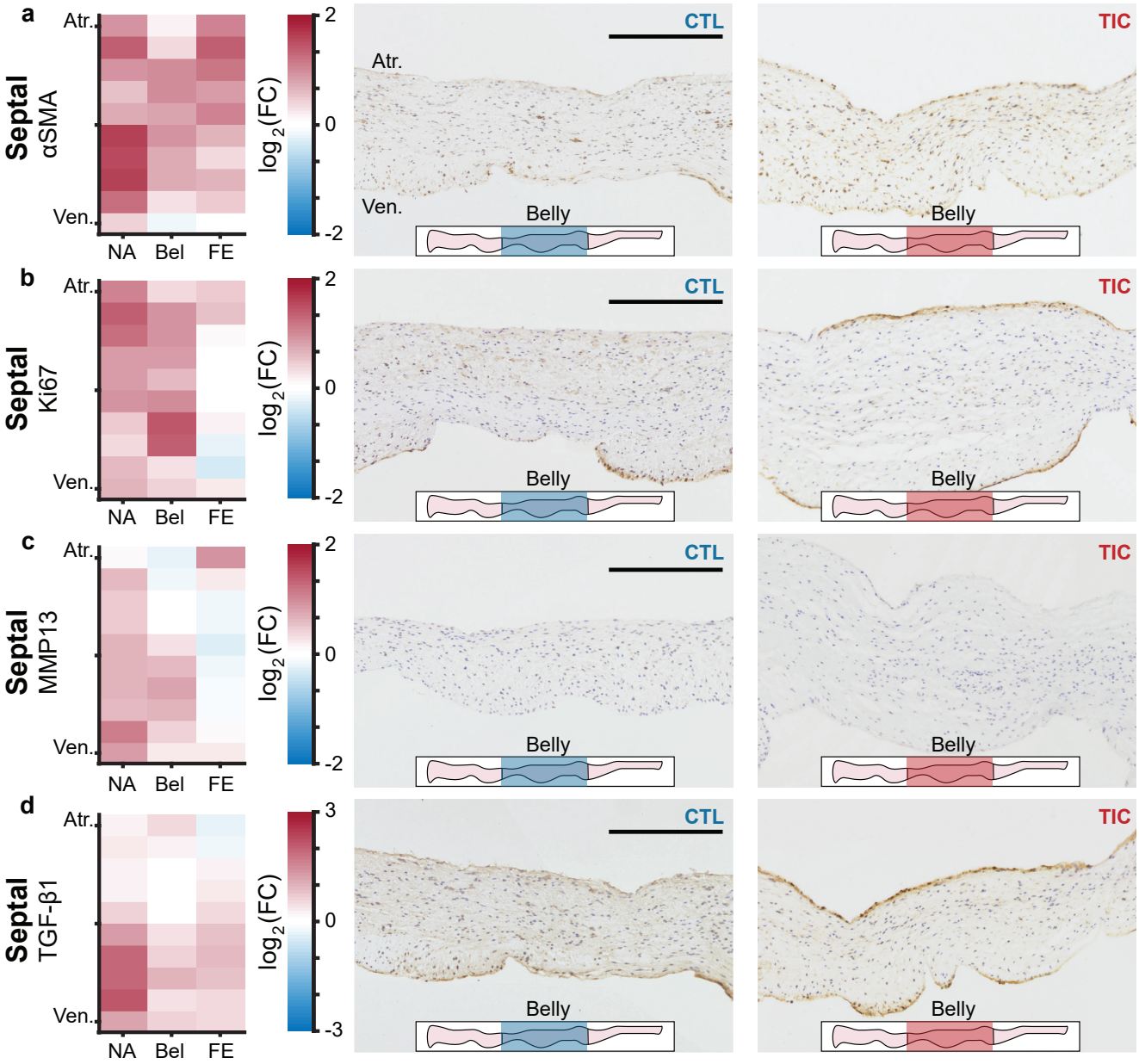

Figure 6. Remodeling cellular markers increase in tachycardia-induced cardiomyopathy (TIC) septal leaflets. (a-d) Heat maps (left) showing regional expression of (a) alpha-smooth muscle actin (αSMA), (b) Ki67, (c) matrix metalloproteinase 13 (MMP13), (d) transforming growth factor beta (TGF-β1). The heatmaps are separated into three equidistant regions along the radial axis (near-annulus (NA), belly (Bel), free edge (FE)) and 10 thickness regions from the atrialis side (Atr.) to the ventricularis side (Ven.). Fold change (FC) between control (CTL, n = 6) and TIC (n = 6) was determined by the ratio of positively stained pixel percentage between TIC and CTL. Color map indicates the logarithm base 2 of the fold change, interpreted as (positive, red): TIC expression is higher than CTL, (0, white): TIC and CTL expression are approximately equal, and (negative, blue): TIC expression is less than CTL. Representative images of CTL (middle) and TIC(right) septal leaflets are shown with the atrialis surface upward. The inset leaflet schematic depicts the longitudinal region from which the representative image was taken. Scale bars = 500 μm.

Figure 6—figure supplement 1. Cellular nuclei density increases along the atrialis surface of the near-annulus region of septal TIC leaflets.

ings for the posterior leaflet. The increased collagen content and predominant circumferential orientation of collagen fibers in the TIC posterior leaflet belly region may account for the increased circumferential stiffness. In contrast, the mechanical results for the septal leaflet do not match our microstructural observations. While collagen fiber dispersion increased in the TIC septal leaflet, this was not reflected in our tissue anisotropy measurements. However, we observed elevated MMP13 signaling in the near-annulus and belly regions, indicating increased collagen degradation and matrix turnover. Therefore, the septal leaflet exhibits more variability in its remodeling response, suggesting that heterogeneous remodeling within the leaflet may play a larger role in driving the mechanical behavior of septal leaflets in diseased subjects.

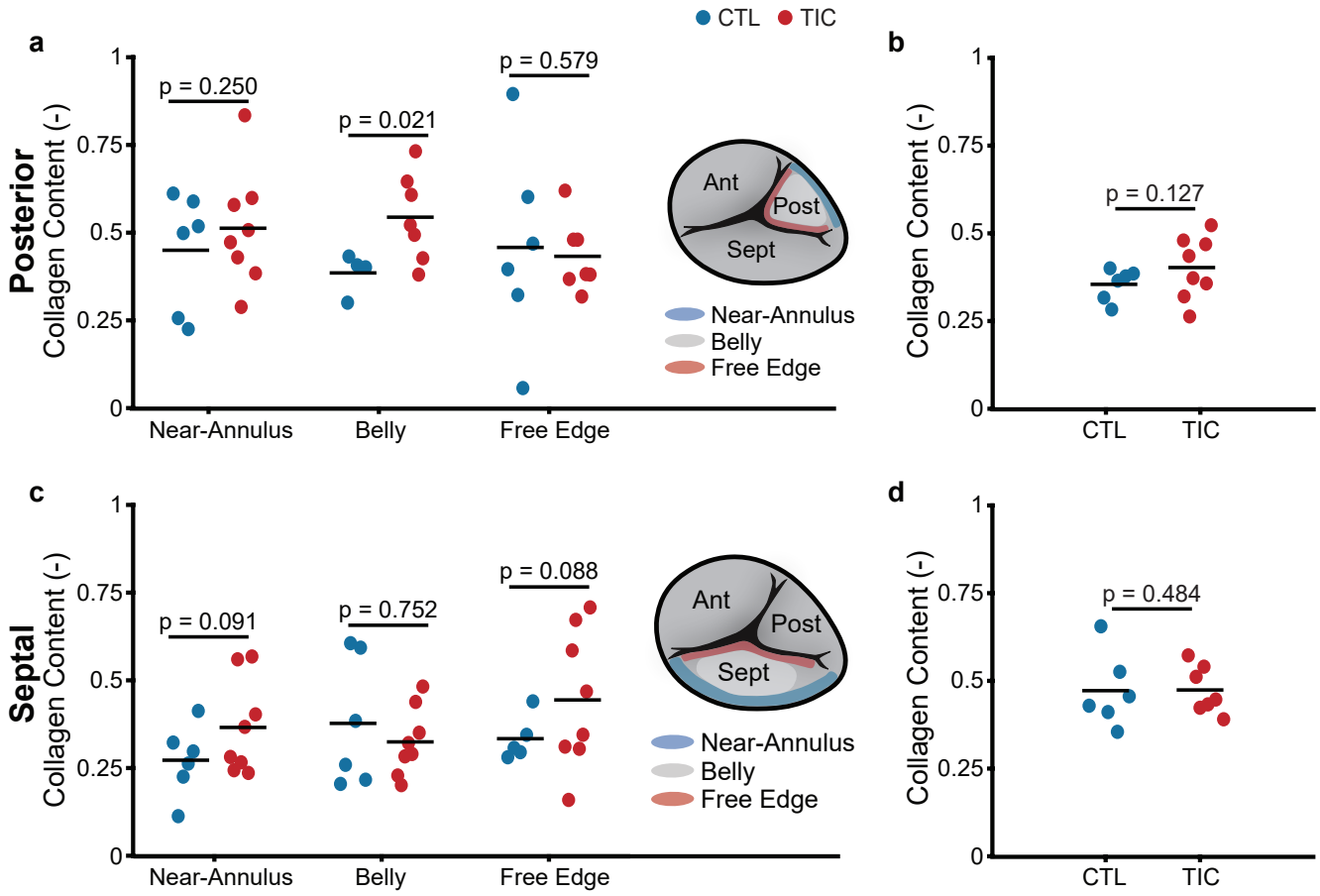

Figure 7. Normalized collagen content increases in tachycardia-induced cardiomyopathy (TIC) posterior leaflets belly region. Regional comparisons of collagen content normalized to total protein content between control (CTL, blue, n = 6 for each leaflet) and TIC (red, n = 8 for each leaflet) for (a)posterior and (c) septal leaflets. Pooled collagen content normalized to total protein content averaged across all regions for (b) posterior and (d) septal leaflets. Black bars represent the data mean if normal and the data median in non-normal as determined by Shapiro-Wilk's normality test. The p-values compare collagen content between CTL and TIC for respective posterior and septal leaflets using the Student's t-test when normally distributed or the Wilcoxon Rank-Sum test when non-normally distributed.

Conclusions

Our study highlights the heterogeneous (mal)adaptive response of the tricuspid valve leaflets in a sheep model of tachycardia-induced biventricular heart failure across several functional scales. Based on our previous study, the anterior leaflet exhibited the greatest remodeling response, while here, we found that the posterior and septal leaflets showed similar but less pronounced changes (***Meador et al., 2020b***). This indicates that the differential biomechanical stimuli observed in these TIC animals influence each leaflet's propensity to remodel (***Iwasieczko et al., 2023b***). These insights

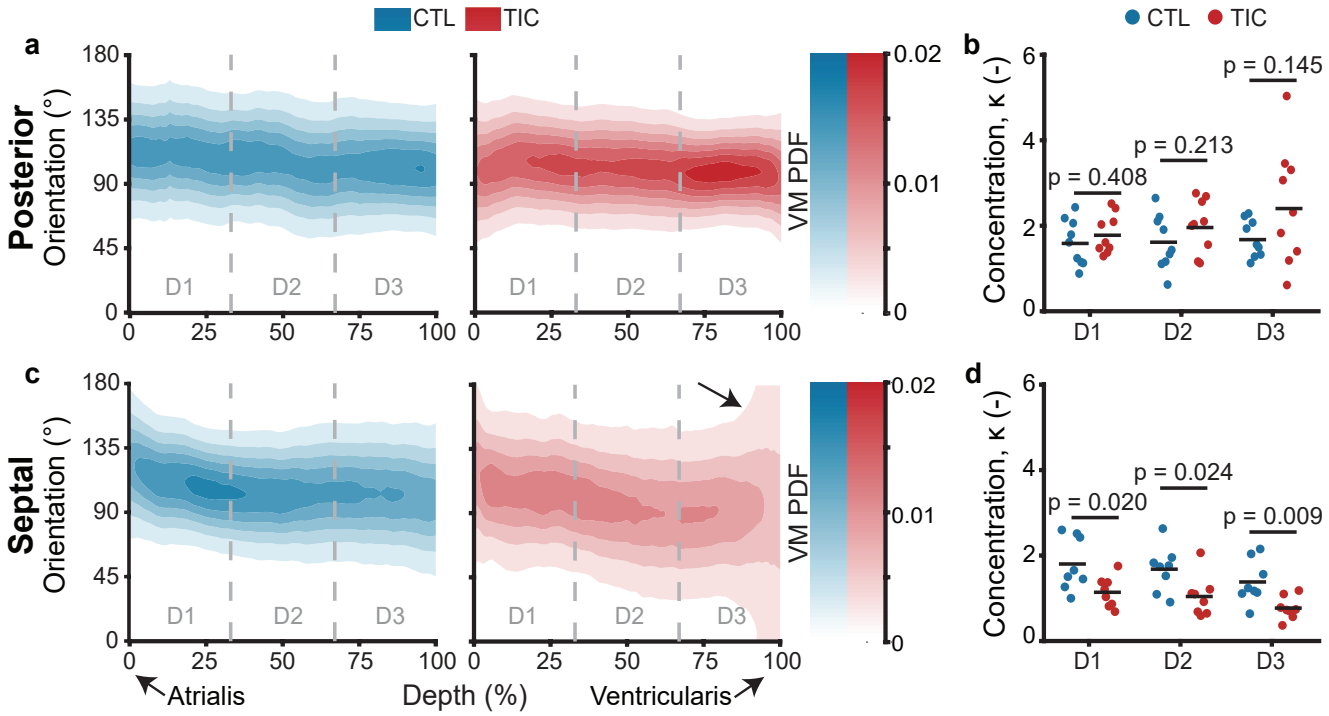

Figure 8. Through-depth collagen microstructure reveals similar mean orientations and regional concentration changed throughout depth between control (CTL) and tachycardia-induced cardiomyopathy (TIC) posterior and septal leaflets. Heat map visualizations of von Mises probability distribution functions (VM PDF) fit to collagen fiber orientation histograms of two-photon acquired images throughout the entire depth (0% - Atrialis surface, 100% - Ventricularis surface) of averaged CTL (blue, n = 9 for each leaflet) and TIC (red, n = 9 for each leaflet) (a) posterior and (c) septal leaflets. Comparisons of VM concentration parameter, κ, across depth regions D1, D2, and D3 for the (b) posterior and (d) septal leaflets. Black bars represent the data mean if normal and the data median in non-normal as determined by Shapiro-Wilk's normality test. The p-values compare circumferential and radial transition stretches and the VM concentration between CTL and TIC for respective posterior and septal leaflets using the Student's t-test when normally distributed or the Wilcoxon Rank-Sum test when non-normally distributed.

Figure 8—figure supplement 1. Heatmap visualizations of nuclei orientation, nuclear aspect ratio (NAR), and circularity of control and tachycardia-induced cardiomyopathy posterior leaflets.

Figure 8—figure supplement 2. Heatmap visualizations of nuclei orientation, nuclear aspect ratio (NAR), and circularity of control and tachycardia-induced cardiomyopathy septal leaflets.

are crucial for directing surgical or pharmacological treatments of tricuspid regurgitation toward a regionally targeted approach.

Incorporating these findings into future computational models can significantly enhance our understanding of valvular disease progression, potentially leading to more clinically relevant results. Computational models, informed by the differential remodeling responses observed in the tricuspid valve leaflets, can help simulate various disease scenarios and predict the impact of different therapeutic interventions (***Mathur et al., 2024***; ***Haese et al., 2024***). This approach can allow for a better understanding of the underlying mechanisms driving leaflet-specific remodeling and aid in developing more precise and effective treatment strategies.

While our findings provide valuable insights into tricuspid valve leaflet remodeling, there are limitations to consider. Our model induces heart failure within weeks, reflecting early adaptive responses rather than the long-term remodeling processes typical in clinical settings. Future studies should extend the study duration to capture chronic remodeling. Additionally, while most data were collected concurrently, 8 new samples were included, potentially introducing batch effects. Despite these limitations, our findings provide valuable insights and directions for future research in tricuspid valve pathology.

In conclusion, our study employed various experimental approaches to reveal the posterior

and septal leaflets' propensity to (mal)adapt across multiple scales. While the posterior leaflet exhibited signs of (mal)adaptive remodeling, the septal leaflet showed remodeling patterns consistent with the anterior leaflet. In the TIC posterior leaflet, we observed: (i) increased free edge thickness, (ii) increased stiffness, (iii) increased regional expression of αSMA and Ki67, and (iv) increased regional collagen content. In the TIC septal leaflet, we observed: (i) increased leaflet area, (ii) increased free edge thickness, (iii) anisotropic mechanical behavior, (iv) increased expression of αSMA, Ki67, MMP13, and TGFβ-1, and (v) increased collagen dispersion. Overall, our findings indicate differential remodeling between and within the tricuspid valve leaflets.

Methods and Materials

Animal model, medication, and procedures

The TIC sheep model used in this study has been previously described in detail and validated as a reliable and repeatable model of biventricular heart failure in sheep (***Malinowski et al., 2017***). The posterior and septal leaflets tested in this study were taken from the same animal cohort as the anterior leaflet. A detailed description of the animal model, medications, and procedures is fully described in our previous published work (***Meador et al., 2020b***). Adult male Dorsett sheep were randomly assigned to either the CTL (n = 17, 59.9 $\pm$ 4.6 kg) or TIC (n = 33, 60.1 $\pm$ 5.3 kg) groups. The TIC animals were subject to a 180-260 beats per minute pacing protocol for 19 ± 6 days. After this, the terminal procedure was performed to excise the tricuspid valve from each animal for further testing.

Morphology and storage

The tricuspid valve leaflet complex was isolated from each heart, and the leaflets were separated at the posterior-septal commissure. Each valve was floated on $1\times$ PBS and imaged on a calibrated grid to compare morphological measures such as leaflet area, major cusp height, and major cusp width between CTL and TIC animals ***Figure 1***a. The leaflets were then separated and cryopreserved in a standard cryomedia containing 10% DMSO supplemented with a protease inhibitor and stored at $-80\,^{\circ}\mathrm{C}$ until tested. Cryogenic studies have shown that the mechanical properties of soft tissues were minimally impacted after storage at temperatures below $0\,^{\circ}\mathrm{C}$ (***Kostelnik et al., 2024***; ***Duginski et al., 2020***).

Thickness, histology, and immunohistochemistry

After thawing, we cut and fixed radial strips (from near-annulus to free edge) of all posterior and septal leaflets in 10% neutral buffered formalin for 24 hours and then transferred to 70% ethanol for long-term storage. We shipped the fixed leaflet strips to the same histological service (HistoServ Inc., Amaranth, MD) for embedding, sectioning ($5\,\mu\mathrm{m}$), and H&E and immunohistochemistry staining. We acquired full section images for all histological and immunohistological sections using a light microscope (Ti2-E High-content Analysis System, Nikon, Tokyo, Japan) with a $10\times$ objective. We used ImageJ (National Institutes of Health, Bethesda, MD, USA) to measure the total length of the tissue section along the atrialis surface and separated each section into three equidistant regions (i.e., near-annulus, belly, and free edge). We then measured the normal vectors between the atrialis and ventricularis surfaces at three random positions within each region, calculated an average regional thickness, and averaged the regional thickness for a sample into the total leaflet thickness.

We assessed the same four cellular markers associated with remodeling processes as what was previously used on the anterior leaflet: (i) alpha-smooth muscle actin (Abcam, ab5694, 1:600, Cambridge, MA, US), (ii) Ki67 (Abcam, ab15580, 1:1250, Cambridge, MA, US), (iii) matrix-metalloprotease 13 (MMP13) (Abcam, ab39012, 1:50, Cambridge, MA, US), and (iv) transforming growth factor β-1 (TGFβ-1) (Abcam, ab9758, 1:100, Cambridge, MA, US). We used our custom MATLAB program to segment the full cross-sectional leaflet image into the same three equidistant length regions (i.e., near-annulus, belly, and free edge) and interpolated ten thickness regions between the atrialis and

ventricularis surfaces for a total of 30 regions. We then passed each region through our custom-validated MATLAB program to spatially resolve the presence of the positive pixels and normalize the percentage of positive pixels to the total pixels in that region.

Biaxial testing and analysis

We tested leaflet samples and analyzed the biaxial mechanics using the methods fully described in our prior work (***Meador et al., 2020a***,b). We isolated a 7×7 mm square sample from the belly region of each posterior and septal leaflet and applied four fiducial markers to the atrialis surface of each sample to enable strain tracking during testing. We measured sample thickness at four locations using a digital thickness gauge (547-500S, Mitutoyo Corp., Kawasaki, Japan) and captured an image of the stress-free configuration on a calibrated grid. All samples were mounted on a biaxial testing device (Biotester, CellScale, Waterloo, ON, Canada), submerged in $37\,^{\circ}\mathrm{C}$ $1\times$ PBS. Next, we performed ten preconditioning cycles of equibiaxial extension to 300 mN and then conducted two final equibiaxial cycles to 300 mN. While testing, we continuously captured circumferential and radial forces and images of the fiducial markers at 5 Hz. All biaxial tests were performed within four hours of thawing. We used the image analysis software Labjoy (CellScale, Waterloo, ON, Canada) to track the coordinates of the fiducial markers throughout testing. In our analysis, we only included the downstroke of the last loading cycle and reported membrane tension-stretch data relative to the preloaded stress-free configuration. To quantitatively compare the nonlinear membrane tension-stretch curves between CTL and TIC for the posterior and septal leaflets, we compared the same four characteristic parameters as the anterior leaflet: toe stiffness, calf stiffness, transition stretch, and anisotropy index. (***Meador et al., 2020b***).

Quantitative collagen assay

We isolated tissue samples from the near-annulus, belly, and free edge regions of each posterior and septal leaflet and measured the wet mass. We used a $1:10$ ratio of tissue to deionized water and homogenized the tissue samples in a bead-mill homogenizer (VWR). We then diluted the tissue homogenates $1:10$ in deionized water to ensure the absorbance measurement was within the standard curve. We followed the protocols provided with a total collagen assay kit (Abcam, ab222942, Cambridge, MA, US) and measured the colorimetric absorbance at 560 nm with a spectrophotometer (Tecan, Infitite 200 Pro, Männedorf, Switzerland). All samples were analyzed in duplicate, and the collagen concentration was interpolated from a collagen type 1 standard linear-fit curve ($R^2 = 0.99 \pm 0.01$). Additionally, we determined the total protein concentration of each sample using a Pierce™Microplate BCA Protein Assay Kit (Thermo Fisher Scientific, 23252, Waltham, MA, USA) to calculate the normalized collagen content.

Two-photon microscopy

We imaged and analyzed the collagen microstructure and cell nuclei using the same two-photon microscopy methods as described in our previous work (***Meador et al., 2020a***). The mechanically tested square sample from the leaflet belly was briefly stained with Hoechst 33342 (Waltham, MA, USA) for 20 minutes to visualize the cell nuclei. The tissue sample was then optically cleared under sonication for 30 minutes in a solution containing glycerol:DMSO:5×PBS at 50:30:20% (v/v), respectively. Next, we imaged the leaflet samples from each group with a two-photon microscope (Ultima IV, Bruker, Billerica, MA, USA) to visualize collagen fiber orientation via second harmonic generation (SHG) and cell nuclei via fluorescent excitation, respectively. The leaflet samples were placed on a foil-lined glass slide with a coverslip placed on top to flatten the sample during imaging while not imposing any stresses. We captured images from the atrialis surface to the ventricularis surface at three centrally located regions (500×500 μm, for each region) using a $20\times$ water-immersion object. We used excitation wavelengths of 900 nm for SHG and 800 nm for fluorescence with linear polarization. We epi-collected the backscattered SHG signal through a PMT channel filter (460 nm $\pm$ 25 nm) and acquired a z-stack of images at a step size of 10 μm. To analyze the SHG images, we used

the orientation distribution analysis with the Gaussian gradient method in the ImageJ plugin OrientationJ (National Institutes of Health, Bethesda, MD, USA). We averaged and interpolated across the three z-stacks for each leaflet sample and then fit a symmetric von Mises distribution to each histogram to estimate the mean fiber angle μ and the fiber orientation concentration κ (***Schriefl et al., 2012***). To analyze the cell nuclei morphology and orientation, we used our custom-validated MATLAB code to quantify individual nuclei contours, nuclear aspect ratio (NAR), and circularity from each image (***Meador et al., 2020a***). In a similar manner, we fit von Mises distributions to the nuclear orientation histograms, while we fit normal distributions to the NAR and circularity histograms.

Statistical analyses

We first performed Shapiro-Wilk tests on all experimental data sets to determine whether the data were normally distributed and F-tests to determine whether the variances of our datasets were similar. We then used a Student's t-test if data were normally distributed and variances were equal, and we used the Wilcoxon Rank-Sum Test or Welch's t-test when appropriate if these assumptions were not met. For statistical comparisons, we used either a one-tailed or two-tailed test, as appropriate, with our stated hypothesis. For all tests, we considered a $p < 0.05$ as statistically significant. All statistical comparisons and correlations were completed in MATLAB.

Acknowledgments

The research reported in this publication was partially supported by the National Heart, Lung, And Blood Institute of the National Institutes of Health under Award Numbers 1R01HL165251-01 (MKR), F31HL145976 (WDM), the American Heart Association for their support under Award Number 18CDA34120028 (MKR), and internal grants from Meijer Heart and Vascular Institute at Spectrum Health. The opinions, findings, and conclusions expressed are those of the authors and do not necessarily reflect the official views of the National Institutes of Health or the American Heart Association.

Additional Information

Competing Interests

Manuel K Rausch has a speaking arrangement with Edwards Lifesciences. The other authors have no conflicts to declare.

Funding Sources

MKR acknowledges the partial support from the National Institutes of Health via grants R01HL165251 and R21HL161832. TAT acknowledges the partial support from the National Institutes of Health via grants R01HL165251 and R21HL161832. WDM acknowledges the partial support from the National Institutes of Health via its predoctoral fellowship F31HL145976. MM acknowledges support from the American Heart Association via its predoctoral fellowship 902502.

Author Contributions

Colton J. Kostelnik: Investigation, Data curation, Formal analysis, Visualization, Writing – original draft, Writing – review & editing. **William D. Meador:** Conceptualization, Data curation, Software, Formal analysis, Investigation, Methodology, Writing – original draft, Writing – review & editing. **Chien-Yu Lin:** Investigation, Writing – review & editing. **Mrudang Mathur:** Investigation, Writing – review & editing. **Marcin Malinowski:** Conceptualization, Investigation, Methodology, Writing – review & editing. **Tomasz Jazwiec:** Investigation, Methodology.**Magda L Piekarska:** Writing – review & editing. **Boguslaw Gaweda:** Writing – review & editing. **Zuzanna Malinowska:** Formal analysis. **Tomasz A. Timek:** Conceptualization,Resources, Supervision, Funding acquisition, Writing – review & editing. **Manuel K. Rausch:** Conceptualization, Writing – original draft, Writing – review & editing, Supervision, Funding acquisition.

References

Afilalo J, Grapsa J, Nihoyannopoulos P, Beaudoin J, Gibbs JSR, Channick RN, Langleben D, Rudski LG, Hua L, Handschumacher MD, Picard MH, Levine RA. Leaflet Area as a Determinant of Tricuspid Regurgitation Severity in Patients With Pulmonary Hypertension. Circulation: Cardiovascular Imaging. 2015 May; 8(5):e002714. https://www.ahajournals.org/doi/10.1161/CIRCIMAGING.114.002714, doi: 10.1161/CIRCIMAGING.114.002714.

Blevins TL, Peterson SB, Lee EL, Bailey AM, Frederick JD, Huynh TN, Gupta V, Grande-Allen KJ. Mitral Valvular Interstitial Cells Demonstrate Regional, Adhesional, and Synthetic Heterogeneity. Cells Tissues Organs. 2008; 187(2):113–122. https://www.karger.com/Article/FullText/108582, doi: 10.1159/000108582.

Chaput M, Handschumacher MD, Tournoux F, Hua L, Guerrero JL, Vlahakes GJ, Levine RA. Mitral Leaflet Adaptation to Ventricular Remodeling: Occurrence and Adequacy in Patients With Functional Mitral Regurgitation. Circulation. 2008 Aug; 118(8):845–852. https://www.ahajournals.org/doi/10.1161/CIRCULATIONAHA.107.749440, doi: 10.1161/CIRCULATIONAHA.107.749440.

Condello F, Gitto M, Stefanini GG. Etiology, epidemiology, pathophysiology and management of tricuspid regurgitation: an overview. Reviews in Cardiovascular Medicine. 2021; 22(4):1115. https://imrpress.com/journal/RCM/22/4/10.31083/j.rcm2204122, doi: 10.31083/j.rcm2204122.

Dal-Bianco JP, Aikawa E, Bischoff J, Guerrero JL, Handschumacher MD, Sullivan S, Johnson B, Titus JS, Iwamoto Y, Wylie-Sears J, Levine RA, Carpentier A. Active Adaptation of the Tethered Mitral Valve: Insights Into a Compensatory Mechanism for Functional Mitral Regurgitation. Circulation. 2009 Jul; 120(4):334–342. https://www.ahajournals.org/doi/10.1161/CIRCULATIONAHA.108.846782, doi: 10.1161/CIRCULATIONAHA.108.846782.

Duginski GA, Ross CJ, Laurence DW, Johns CH, Lee CH. An investigation of the effect of freezing storage on the biaxial mechanical properties of excised porcine tricuspid valve anterior leaflets. Journal of the Mechanical Behavior of Biomedical Materials. 2020 Jan; 101:103438. https://linkinghub.elsevier.com/retrieve/pii/S1751616119307416, doi: 10.1016/j.jmbbm.2019.103438.

Enriquez-Sarano M, Messika-Zeitoun D, Topilsky Y, Tribouilloy C, Benfari G, Michelena H. Tricuspid regurgitation is a public health crisis. Progress in Cardiovascular Diseases. 2019 Nov; 62(6):447–451. https://linkinghub.elsevier.com/retrieve/pii/S0033062019301343, doi: 10.1016/j.pcad.2019.10.009.

Fender EA, Zack CJ, Nishimura RA. Isolated tricuspid regurgitation: outcomes and therapeutic interventions. Heart. 2018 May; 104(10):798–806. https://heart.bmj.com/lookup/doi/10.1136/heartjnl-2017-311586, doi: 10.1136/heartjnl-2017-311586.

Grande-Allen KJ, Barber JE, Klatka KM, Houghtaling PL, Vesely I, Moravec CS, McCarthy PM. Mitral valve stiffening in end-stage heart failure: Evidence of an organic contribution to functional mitral regurgitation. The Journal of Thoracic and Cardiovascular Surgery. 2005 Sep; 130(3):783–790. https://linkinghub.elsevier.com/retrieve/pii/S0022522305006975, doi: 10.1016/j.jtcvs.2005.04.019.

Grande-Allen KJ, Borowski AG, Troughton RW, Houghtaling PL, DiPaola NR, Moravec CS, Vesely I, Griffin BP. Apparently normal mitral valves in patients with heart failure demonstrate biochemical and structural derangements. Journal of the American College of Cardiology. 2005 Jan; 45(1):54–61. https://linkinghub.elsevier.com/retrieve/pii/S0735109704019576, doi: 10.1016/j.jacc.2004.06.079.

Grande-Allen KJ, Liao J. The Heterogeneous Biomechanics and Mechanobiology of the Mitral Valve: Implications for Tissue Engineering. Current Cardiology Reports. 2011 Apr; 13(2):113–120. http://link.springer.com/10.1007/s11886-010-0161-2, doi: 10.1007/s11886-010-0161-2.

Haese CE, Mathur M, Lin CY, Malinowski M, Timek TA, Rausch MK. Impact of tricuspid annuloplasty device shape and size on valve mechanics—a computational study. JTCVS Open. 2024 Feb; 17:111–120. https://linkinghub.elsevier.com/retrieve/pii/S2666273623003534, doi: 10.1016/j.xjon.2023.11.002.

Henning RJ. Tricuspid valve regurgitation: current diagnosis and treatment. American Journal of Cardiovascular Disease. 2022 Feb; 12(1):1–18.

Hudson LT, Jett SV, Kramer KE, Laurence DW, Ross CJ, Towner RA, Baumwart R, Lim KM, Mir A, Burkhart HM, Wu Y, Lee CH. A Pilot Study on Linking Tissue Mechanics with Load-Dependent Collagen Microstructures in Porcine Tricuspid Valve Leaflets. Bioengineering. 2020 Jun; 7(2):60. https://www.mdpi.com/2306-5354/7/2/60, doi: 10.3390/bioengineering7020060.

Itoh A, Krishnamurthy G, Swanson JC, Ennis DB, Bothe W, Kuhl E, Karlsson M, Davis LR, Miller DC, Ingels NB. Active stiffening of mitral valve leaflets in the beating heart. American Journal of Physiology-Heart and Circulatory Physiology. 2009 Jun; 296(6):H1766–H1773. https://www.physiology.org/doi/10.1152/ajpheart.00120.2009, doi: 10.1152/ajpheart.00120.2009.

Iwasieczko A, Gaddam M, Gaweda B, Goodyke A, Mathur M, Lin CY, Zagorski J, Solarewicz M, Cohle S, Rausch M, Timek TA. Valvular complex and tissue remodelling in ovine functional tricuspid regurgitation. European Journal of Cardio-Thoracic Surgery. 2023 May; 63(5):ezad115. https://academic.oup.com/ejcts/article/doi/10.1093/ejcts/ezad115/7084775, doi: 10.1093/ejcts/ezad115.

Iwasieczko A, Jazwiec T, Gaddam M, Gaweda B, Piekarska M, Solarewicz M, Rausch MK, Timek TA. Septal annular dilation in chronic ovine functional tricuspid regurgitation. The Journal of Thoracic and Cardiovascular Surgery. 2023 Nov; 166(5):e393–e403. https://linkinghub.elsevier.com/retrieve/pii/S0022522323003240, doi: 10.1016/j.jtcvs.2023.04.003.

Kodigepalli KM, Thatcher K, West T, Howsmon DP, Schoen FJ, Sacks MS, Breuer CK, Lincoln J. Biology and Biomechanics of the Heart Valve Extracellular Matrix. Journal of Cardiovascular Development and Disease. 2020 Dec; 7(4):57. https://www.mdpi.com/2308-3425/7/4/57, doi: 10.3390/jcdd7040057.

Korossis S. Structure-Function Relationship of Heart Valves in Health and Disease. In: Kirali K, editor. *Structural Insufficiency Anomalies in Cardiac Valves* InTech; 2018.http://www.intechopen.com/books/structural-insufficiency-anomalies-in-cardiac-valves/structure-function-relationship-of-heart-valves-in-health-and-disease, doi: 10.5772/intechopen.78280.

Kostelnik CJ, Crouse KJ, Goldsmith JD, Eberth JF. Impact of cryopreservation on elastomuscular artery mechanics. Journal of the Mechanical Behavior of Biomedical Materials. 2024 Jun; 154:106503. https://linkinghub.elsevier.com/retrieve/pii/S1751616124001358, doi: 10.1016/j.jmbbm.2024.106503.

Laurence D, Ross C, Jett S, Johns C, Echols A, Baumwart R, Towner R, Liao J, Bajona P, Wu Y, Lee CH. An investigation of regional variations in the biaxial mechanical properties and stress relaxation behaviors of porcine atrioventricular heart valve leaflets. Journal of Biomechanics. 2019 Jan; 83:16–27. https://linkinghub.elsevier.com/retrieve/pii/S0021929018308509, doi: 10.1016/j.jbiomech.2018.11.015.

Lee CH, Laurence DW, Ross CJ, Kramer KE, Babu AR, Johnson EL, Hsu MC, Aggarwal A, Mir A, Burkhart HM, Towner RA, Baumwart R, Wu Y. Mechanics of the Tricuspid Valve—From Clinical Diagnosis/Treatment, In-Vivo and In-Vitro Investigations, to Patient-Specific Biomechanical Modeling. Bioengineering. 2019 May; 6(2):47. https://www.mdpi.com/2306-5354/6/2/47, doi: 10.3390/bioengineering6020047.

Li Y, Lui KO, Zhou B. Reassessing endothelial-to-mesenchymal transition in cardiovascular diseases. Nature Reviews Cardiology. 2018 Aug; 15(8):445–456. https://www.nature.com/articles/s41569-018-0023-y, doi: 10.1038/s41569-018-0023-y.

Ma H, Killaars AR, DelRio FW, Yang C, Anseth KS. Myofibroblastic activation of valvular interstitial cells is modulated by spatial variations in matrix elasticity and its organization. Biomaterials. 2017 Jul; 131:131–144. https://linkinghub.elsevier.com/retrieve/pii/S0142961217301977, doi: 10.1016/j.biomaterials.2017.03.040.

Malinowski M, Proudfoot AG, Langholz D, Eberhart L, Brown M, Schubert H, Wodarek J, Timek TA. Large animal model of functional tricuspid regurgitation in pacing induced end-stage heart failure. Interactive CardioVascular and Thoracic Surgery. 2017 Jun; 24(6):905–910. https://academic.oup.com/icvts/article-lookup/doi/10.1093/icvts/ivx012, doi: 10.1093/icvts/ivx012.

Mathur M, Jazwiec T, Meador WD, Malinowski M, Goehler M, Ferguson H, Timek TA, Rausch MK. Tricuspid valve leaflet strains in the beating ovine heart. Biomechanics and Modeling in Mechanobiology. 2019 Oct; 18(5):1351–1361. http://link.springer.com/10.1007/s10237-019-01148-y, doi: 10.1007/s10237-019-01148-y.

Mathur M, Malinowski M, Jazwiec T, Timek TA, Rausch MK. Leaflet remodeling reduces tricuspid valve function in a computational model. Journal of the Mechanical Behavior of Biomedical Materials. 2024 Apr; 152:106453. https://linkinghub.elsevier.com/retrieve/pii/S1751616124000857, doi: 10.1016/j.jmbbm.2024.106453.

Meador WD, Mathur M, Sugerman GP, Jazwiec T, Malinowski M, Bersi MR, Timek TA, Rausch MK. A detailed mechanical and microstructural analysis of ovine tricuspid valve leaflets. Acta Biomaterialia. 2020 Jan; 102:100–113. https://linkinghub.elsevier.com/retrieve/pii/S1742706119307895, doi: 10.1016/j.actbio.2019.11.039.

Meador WD, Mathur M, Sugerman GP, Malinowski M, Jazwiec T, Wang X, Lacerda CM, Timek TA, Rausch MK. The tricuspid valve also maladapts as shown in sheep with biventricular heart failure. eLife. 2020 Dec; 9:e63855. https://elifesciences.org/articles/63855, doi: 10.7554/eLife.63855.

Pagnesi M, Montalto C, Mangieri A, Agricola E, Puri R, Chiarito M, Ancona MB, Regazzoli D, Testa L, De Bonis M, Moat NE, Rodés-Cabau J, Colombo A, Latib A. Tricuspid annuloplasty versus a conservative approach in patients with functional tricuspid regurgitation undergoing left-sided heart valve surgery: A study-level meta-analysis. International Journal of Cardiology. 2017 Aug; 240:138–144. https://linkinghub.elsevier.com/retrieve/pii/S016752731732140X, doi: 10.1016/j.ijcard.2017.05.014.

Rausch MK, Tibayan FA, Craig Miller D, Kuhl E. Evidence of adaptive mitral leaflet growth. Journal of the Mechanical Behavior of Biomedical Materials. 2012 Nov; 15:208–217. https://linkinghub.elsevier.com/retrieve/pii/S1751616112001944, doi: 10.1016/j.jmbbm.2012.07.001.

Rogers JH, Bolling SF. The Tricuspid Valve: Current Perspective and Evolving Management of Tricuspid Regurgitation. Circulation. 2009 May; 119(20):2718–2725. https://www.ahajournals.org/doi/10.1161/CIRCULATIONAHA.108.842773, doi: 10.1161/CIRCULATIONAHA.108.842773.

Schriefl AJ, Reinisch AJ, Sankaran S, Pierce DM, Holzapfel GA. Quantitative assessment of collagen fibre orientations from two-dimensional images of soft biological tissues. Journal of The Royal Society Interface. 2012 Nov; 9(76):3081–3093. https://royalsocietypublishing.org/doi/10.1098/rsif.2012.0339, doi: 10.1098/rsif.2012.0339.

Singh JP, Evans JC, Levy D, Larson MG, Freed LA, Fuller DL, Lehman B, Benjamin EJ. Prevalence and clinical determinants of mitral, tricuspid, and aortic regurgitation (the Framingham Heart Study). The American Journal of Cardiology. 1999 Mar; 83(6):897–902. https://linkinghub.elsevier.com/retrieve/pii/S0002914998010649, doi: 10.1016/S0002-9149(98)01064-9.

Stephens EH, Timek TA, Daughters GT, Kuo JJ, Patton AM, Baggett LS, Ingels NB, Miller DC, Grande-Allen KJ. Significant Changes in Mitral Valve Leaflet Matrix Composition and Turnover With Tachycardia-Induced Cardiomyopathy. Circulation. 2009 Sep; 120(11_suppl_1). https://www.ahajournals.org/doi/10.1161/CIRCULATIONAHA.108.844159, doi: 10.1161/CIRCULATIONAHA.108.844159.

Taramasso M, Vanermen H, Maisano F, Guidotti A, La Canna G, Alfieri O. The Growing Clinical Importance of Secondary Tricuspid Regurgitation. Journal of the American College of Cardiology. 2012 Feb; 59(8):703–710. https://linkinghub.elsevier.com/retrieve/pii/S0735109711050984, doi: 10.1016/j.jacc.2011.09.069.

Timek TA, Lai DT, Dagum P, Liang D, Daughters GT, Ingels NB, Miller DC. Mitral Leaflet Remodeling in Dilated Cardiomyopathy. Circulation. 2006 Jul; 114(1_supplement). https://www.ahajournals.org/doi/10.1161/CIRCULATIONAHA.105.000554, doi: 10.1161/CIRCULATIONAHA.105.000554.

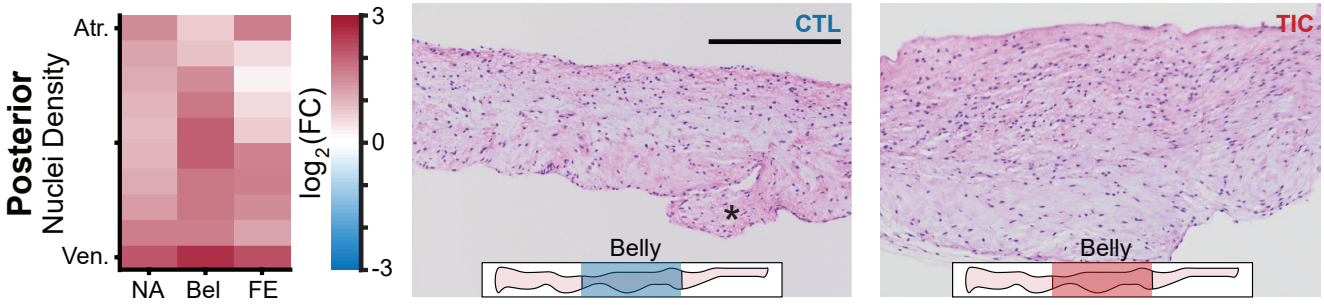

Figure 5—figure supplement 1. Heatmap (left) showing regional cell nuclei density of hematoxylin-eosin stained posterior control (CTL)(middle) and tachycardia-induced cardiomyopathy (TIC) (right) leaflets. The heatmaps are separated into three equistant longitudinal regions along the leaflet's radial axis (near-annulus) (NA), belly, and free edge (FE)) and 10 thickness region from the atrialis surface (Atr.) to the ventricularis surface (Ven.) Fold change (FC) between CTL (n = 6) and TIC (n = 6) was determined by the ratio of cell nuclei count between TIC and CTL. Color map indicates the logarithm base 2 of the fold change, interpreted as (positive, red): TIC expression is higher than CTL, (0, white): TIC and CTL expression are approximately equal, and (negative, blue): TIC expression is less than CTL. Representative images of CTL (middle) and TIC(right) posterior leaflets are shown with the atrialis surface upward. Asterisk (*) denotes chordae tendineae which was excluded from the analysis. The inset leaflet schematic depicts the longitudinal region from which the representative image was taken. Scale bars = $500\ \mu$m.

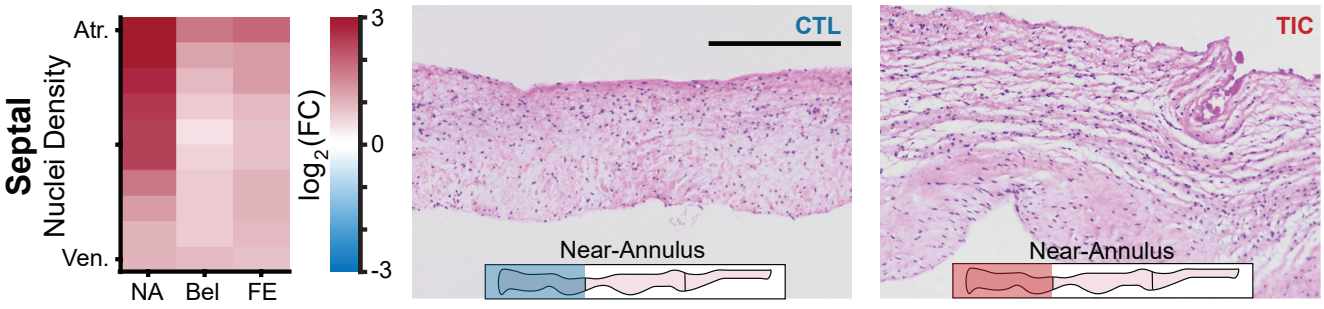

Figure 6—figure supplement 1. Heatmap (left) showing regional cell nuclei density of hematoxylin-eosin stained septal control (CTL)(middle) and tachycardia-induced cardiomyopathy (TIC) (right) leaflets. The heatmaps are separated into three equidistant longitudinal regions along the leaflet's radial axis (near-annulus) (NA), belly, and free edge (FE)) and ten thickness regions from the atrialis surface (Atr.) to the ventricularis surface (Ven.) Fold change (FC) between CTL (n = 6) and TIC (n = 6) was determined by the ratio of cell nuclei count between TIC and CTL. Color map indicates the logarithm base 2 of the fold change, interpreted as (positive, red): TIC expression is higher than CTL, (0, white): TIC and CTL expression are approximately equal, and (negative, blue): TIC expression is less than CTL. Representative images of CTL (middle) and TIC(right) septal leaflets are shown with the atrialis surface upward. The inset leaflet schematic depicts the longitudinal region from which the representative image was taken. Scale bars = 500 μm.

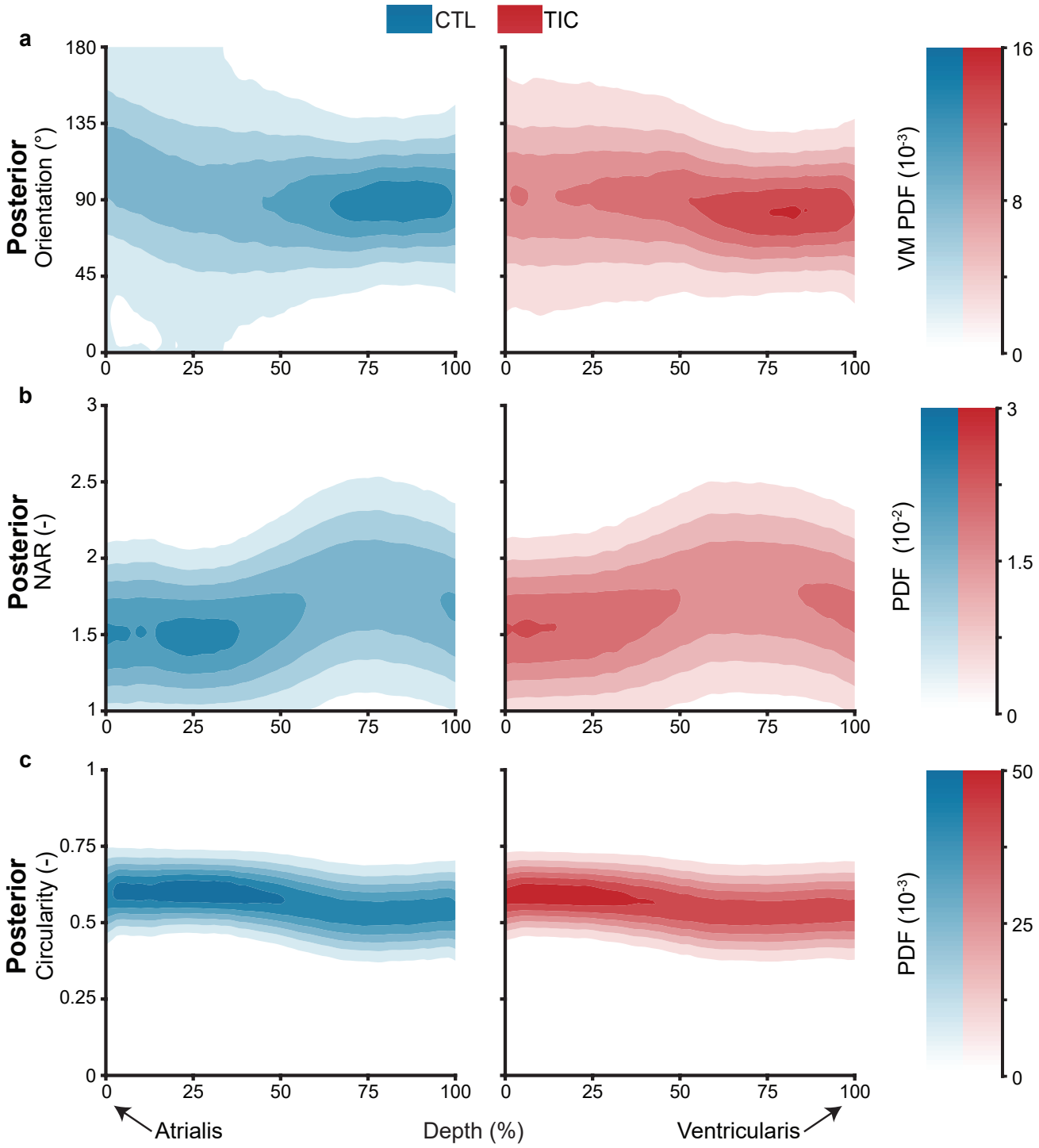

Figure 8—figure supplement 1. Through-depth imaging of nuclei orientation, nuclear aspect ratio (NAR), and circularity of control (blue, n = 9) and tachycardia-induced cardiomyopathy (red, n = 9) posterior leaflets.

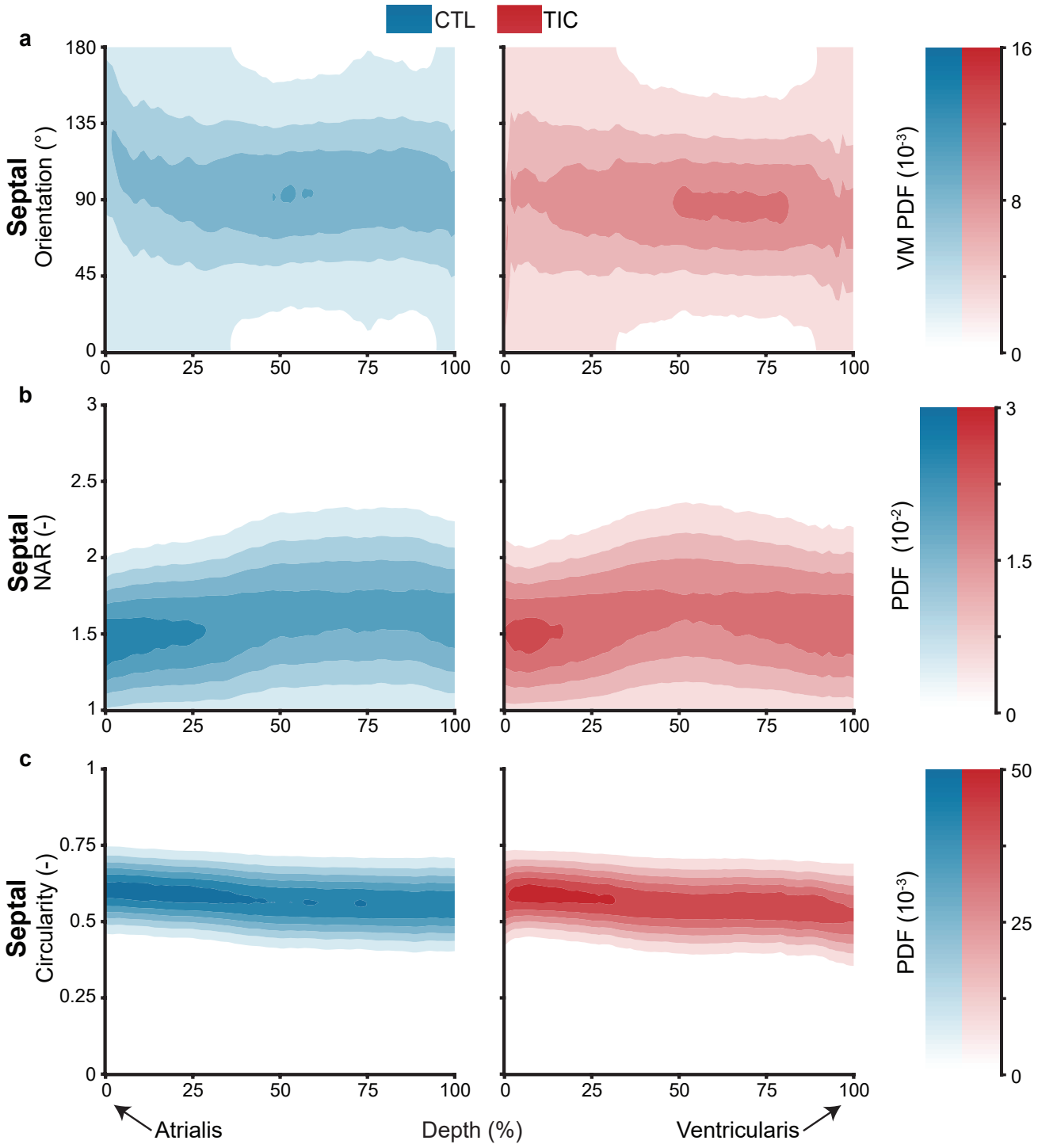

Figure 8—figure supplement 2. Through-depth imaging of nuclei orientation, nuclear aspect ratio (NAR), and circularity of control (blue, n = 9) and tachycardia-induced cardiomyopathy (red, n = 9) septal leaflets.